

## ARTICLE OPEN

Superconductivity in topologically nontrivial material Au<sub>2</sub>PbYing Xing<sup>1,2,5</sup>, He Wang<sup>1,2,5</sup>, Chao-Kai Li<sup>1,2,5</sup>, Xiao Zhang<sup>1,2</sup>, Jun Liu<sup>3</sup>, Yangwei Zhang<sup>1,2</sup>, Jiawei Luo<sup>1,2</sup>, Ziqiao Wang<sup>1,2</sup>, Yong Wang<sup>3</sup>, Langsheng Ling<sup>4</sup>, Mingliang Tian<sup>4</sup>, Shuang Jia<sup>1,2</sup>, Ji Feng<sup>1,2</sup>, Xiong-Jun Liu<sup>1,2</sup>, Jian Wei<sup>1,2</sup> and Jian Wang<sup>1,2</sup>

The search for nontrivial superconductivity in novel quantum materials is currently a most attractive topic in condensed matter physics and material science. The experimental studies have progressed quickly over the past couple of years. In this article, we report systematic studies of superconductivity in Au<sub>2</sub>Pb single crystals. The bulk superconductivity (onset transition temperature,  $T_c^{\text{onset}} = 1.3$  K) of Au<sub>2</sub>Pb is characterised by both transport and diamagnetic measurements, where the upper critical field  $H_{c2}$  shows unusual quasi-linear temperature dependence. The superconducting gap is revealed by point-contact measurement with gold tip. However, when using tungsten (W) tip, which is much harder, the superconducting gap probed is largely enhanced as demonstrated by the increases of both  $T_c^{\text{onset}}$  and upper critical field ( $H_{c2}$ ). This can be interpreted as a result of increase in density of states under external anisotropic stress imposed by the tip, as revealed by first-principles calculations. Furthermore, novel phase winding of the pseudospin texture along k-space loops around the Fermi energy is uncovered from the calculations, indicating that the observed superconductivity in Au<sub>2</sub>Pb may have nontrivial topology.

npj Quantum Materials (2016) 1, 16005; doi:10.1038/npjquantmats.2016.5; published online 27 July 2016

## INTRODUCTION

The recent discovery of three-dimensional (3D) Dirac semimetals,<sup>1–12</sup> as an intermediate state between a trivial insulator and a topological insulator, has stimulated extensive research on these materials. In 3D Dirac semimetals, the conduction and valence bands contact only at Dirac points in the Brillouin zone, and gap formation is forbidden by crystalline symmetry. Much recent excitement has surrounded the materials like Na<sub>3</sub>Bi<sup>2</sup> and Cd<sub>3</sub>As<sub>2</sub>,<sup>3</sup> in which the Dirac cone semimetal states were predicted theoretically and soon identified by Angle-resolved photoemission spectroscopy (ARPES) experiments.<sup>4,6,11</sup> Surprisingly, the superconductivity induced by hard point contact (PC) on Cd<sub>3</sub>As<sub>2</sub> was recently reported and unconventional superconducting order parameter was suggested by the zero-bias conductance peak (ZBCP) and double conductance peaks (DCPs) symmetric around zero bias.<sup>13,14</sup> In addition, pressure-induced superconductivity in Cd<sub>3</sub>As<sub>2</sub> was further confirmed by hydrostatic pressure experiment.<sup>15</sup>

Another promising material is the cubic Laves phase Au<sub>2</sub>Pb, which reveals the signature for the symmetry-protected Dirac semimetal state at temperature > 100 K. However, after the structural phase transition, the Dirac cone is gapped < 100 K.<sup>16</sup> Here we report systematic studies of low-temperature transport and diamagnetic properties, PC measurements and first-principles calculations of Au<sub>2</sub>Pb single crystal. The superconductivity of Au<sub>2</sub>Pb is characterised, and the anomalous quasi-linear  $H_{c2}(T)$  in Au<sub>2</sub>Pb suggests the presence of an unconventional superconducting state. The  $T_c^{\text{onset}}$  and  $H_{c2}$  revealed by the PC measurement with a gold tip is consistent with that by the bulk transport and magnetisation measurements, but with a hard W tip, the gap is largely enhanced as shown by the increases of both  $T_c^{\text{onset}}$  and  $H_{c2}$ . By comparing the computed Fermi surfaces of Au<sub>2</sub>Pb of relaxed lattice structure and those under 1% uniaxial compression, we find that the Fermi surfaces are enlarged and the

density of states near the Fermi energy increases under the applied external pressure, which agrees with the observed increase of  $T_c^{\text{onset}}$  in the PC measurements. More importantly, the possibility of topological superconductivity is suggested by first-principles calculations, which show nontrivial topological properties of the projected pseudospin texture corresponding to the *p*- and *d*-orbitals near the Fermi energy, as well as the experimental observations of anomalous quasi-linear  $H_{c2}(T)$  behaviour and unusual PCS feature detected by W tip. These characteristics make Au<sub>2</sub>Pb a potential candidate material for topological superconductor.

## RESULTS

## Sample structure

High-quality single crystal of Au<sub>2</sub>Pb samples were synthesised by self-flux method in the evacuated quartz ampoule (see Materials and Methods). The powder X-ray diffraction (XRD) pattern is given in Figure 1a, indicating a crystal structure of Au<sub>2</sub>Pb and exhibiting a cubic Laves phase with  $a_1 = a_2 = a_3 = 7.9603$  Å at room temperature. The single crystal XRD pattern only shows (111) reflections, suggesting the sample surface of the crystal is (111) plane (inset of Figure 1a). The atomic high-resolution transmission electron microscopy (HRTEM) image (Figure 1b), together with the selected area electron diffraction pattern (Figure 1c), further demonstrate the high-quality single crystal nature of Au<sub>2</sub>Pb samples.

## Superconductivity

The superconductivity in Au<sub>2</sub>Pb has been confirmed by our systematic low-temperature transport and diamagnetic measurements. Figure 2a displays the sample resistivity ( $\rho$ ) as a function of temperature at zero magnetic field. The behaviour is

<sup>1</sup>International Center for Quantum Materials, School of Physics, Peking University, Beijing, China; <sup>2</sup>Collaborative Innovation Center of Quantum Matter, Beijing, China; <sup>3</sup>Center of Electron Microscopy, State Key Laboratory of Silicon Materials, School of Materials Science and Engineering, Zhejiang University, Hangzhou, China and <sup>4</sup>High Magnetic Field Laboratory, Chinese Academy of Sciences, Anhui, China.

Correspondence: J Feng (jfeng11@pku.edu.cn) or J Wei (weijian6791@pku.edu.cn) or J Wang (jianwangphysics@pku.edu.cn)

<sup>5</sup>These authors contributed equally to this work.

Received 26 May 2016; revised 21 June 2016; accepted 21 June 2016

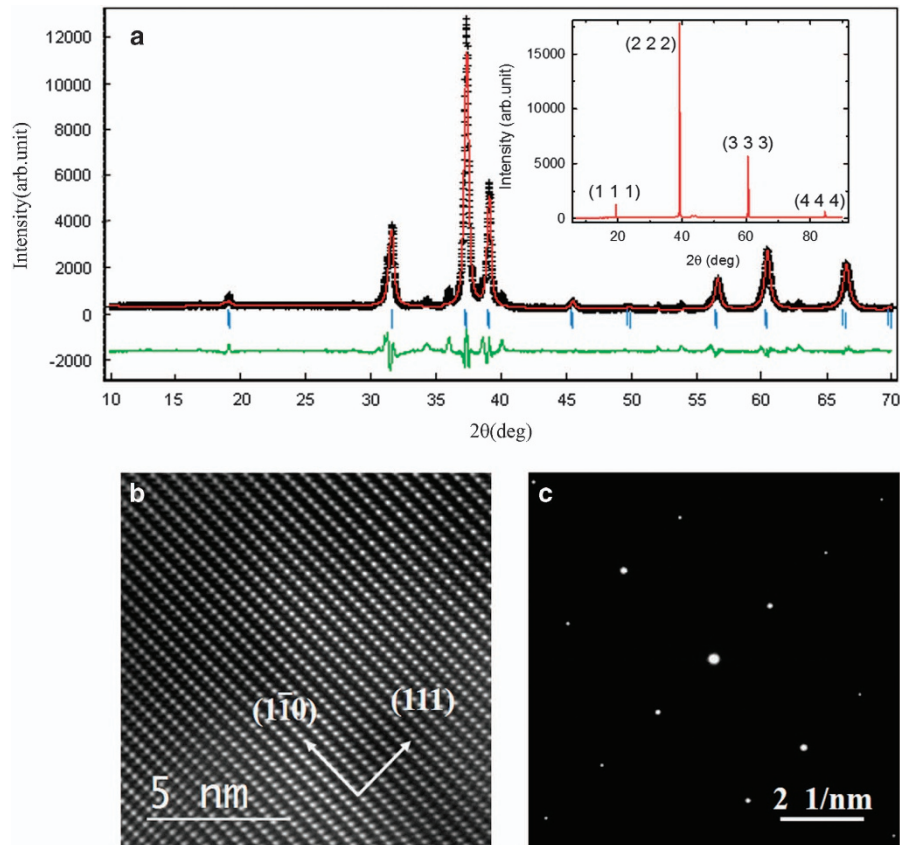


**Figure 1.** Sample characterisation. (a) X-ray diffraction patterns at room temperature for the Au<sub>2</sub>Pb samples. The major diffraction peaks can be indexed with a cubic Laves phase of Au<sub>2</sub>Pb. A few tiny diffraction peaks are from the impurity phases of a small amount of Pb residue. Inset: the X-ray diffraction pattern from the basal plane crystal surface of Au<sub>2</sub>Pb only shows (111)<sub>n</sub> reflections, which indicates the measured crystal plane of the crystal is (111) plane. (b) High-resolution transmission electron microscopy image of Au<sub>2</sub>Pb crystal. (c) Selected area electron diffraction image looking down from the [112] zone axis showing the reciprocal lattice of Au<sub>2</sub>Pb.

metallic with an anomaly of  $\rho(T)$  at 100 K due to a structural phase transition (cubic Laves phase > 100 K).<sup>16</sup> A steep step at 50 K and hysteresis at 40 K are observed with cooling and heating measurements, owing to structural transition to orthorhombic phase < 40 K (the inset of Figure 2a). On cooling down to lower temperature, bulk  $T_c^{\text{onset}} \sim 1.3$  K and zero resistance transition temperature  $T_c^{\text{zero}} \sim 1.18$  K are observed, comparable to the previous reports.<sup>16,17</sup> The superconductivity in Au<sub>2</sub>Pb is further confirmed by Meissner effect measurements. In Figure 2b, the susceptibility ( $\chi$ ) versus temperature curves show quite sharp drops at 1.15 K, in good agreement with  $T_c^{\text{zero}}$  from  $\rho(T)$  curve. Magnetic field dependence of the magnetisation ( $M(H)$ ) curves at various temperatures (inset of Figure 2b) exhibit the expected quasi-linear behaviour at low fields but deviate from linearity above the lower critical field  $H_{c1}$ . Figure 2c reveals the suppression of the superconducting state of Au<sub>2</sub>Pb by the magnetic field perpendicular to (111) plane ( $H_{\perp}$ ). The superconducting transition becomes broader and shifts to lower temperature with increasing fields. Magnetotransport measurements were carried out at various temperatures from 0.18 to 1.4 K (Figure 2d). The onset  $H_{c2}$ , defined as the field above which the Au<sub>2</sub>Pb sample becomes the normal state, is shown in Supplementary Figure S1.  $H_{c2}$  linearly increases with decreasing temperature down to  $T_c/6$ , yields  $dH_{c2}(T)/dT|_{T=T_c} \approx 0.054$  T/K near  $T_c$ . We calculate the reduced critical field  $h^* = H_{c2}/T_c(dH_{c2}/dT|_{T=T_c})$  (inset of Figure 2d) to compare the data to the known models for *s*-wave superconductors (Werthamer–Helfand–Hohenberg theory, WHH,  $H_{c2} \approx 0.7T_c dH_{c2}/dT|_{T=T_c}$ ,  $h^*(0) \approx 0.7$ )<sup>18</sup> and spin-triplet *p*-wave superconductors ( $h^*(0) \approx 0.8$ ).<sup>19</sup> Obviously, the  $h^*$  relation is close

in the form to that of a polar *p*-wave state, which is suggestive of the finite triplet contribution to the pairing state in Au<sub>2</sub>Pb.<sup>19,20</sup> The upper critical field  $H_{c2}(T)$  shows little anisotropic property for perpendicular and parallel magnetic field (Supplementary Figure S2). Furthermore, we plotted the normalized magneto-resistivity ( $MR = (\rho(H) - \rho(0))/\rho(0) \times 100\%$ ) of Au<sub>2</sub>Pb as the field up to 15 T, from 1 to 200 K (see Figure 2e). In contrast to the classical quadratic MR in metals and semiconductors, the sample presents non-saturating linear-like MR at lower temperatures and higher-magnetic fields. With increasing temperatures, the exponent  $\alpha$  ( $MR \propto H^{\alpha}$ ) varies between 1 and 2 and exhibits anomalies when temperatures undergo structural phase transitions  $\sim 40$  K, 100 K (Supplementary Figure S3b). In the parallel field ( $H//$ (111) plane:  $H_{\parallel}$ ) configuration, Figure 2f demonstrates how the MR behaviour changes when the direction of the magnetic field is rotated from  $0^\circ$  ( $H//[\bar{1}\bar{1}2] \perp I$ ) to  $90^\circ$  ( $H//[\bar{1}\bar{1}0] \parallel I$ ) at 2.5 K. Classically, the resistance has no response to the applied external magnetic field parallel to the excitation current. While in our situation, MR is quasi-linear-dependent on magnetic field ( $MR \propto H^{1.09 \pm 0.02}$ , inset of Figure 2f). The linear magnetoresistance behaviour has usually been observed in semiconductor,<sup>21</sup> semimetals,<sup>22</sup> topological insulators<sup>23–25</sup> and Dirac/Weyl semimetals.<sup>10,26,27</sup> One general interpretation is inhomogeneity in materials, but the inhomogeneity does not seem to play an important role here, since our Au<sub>2</sub>Pb crystals show good single crystal quality. Alternatively, it is also tempting to ascribe the linear magnetoresistance to Abrikosov’s quantum magnetoresistance,<sup>28</sup> however, the estimated carrier density  $10^{22}$  cm<sup>-3</sup> (see Supplementary Figure S4) is too high for this

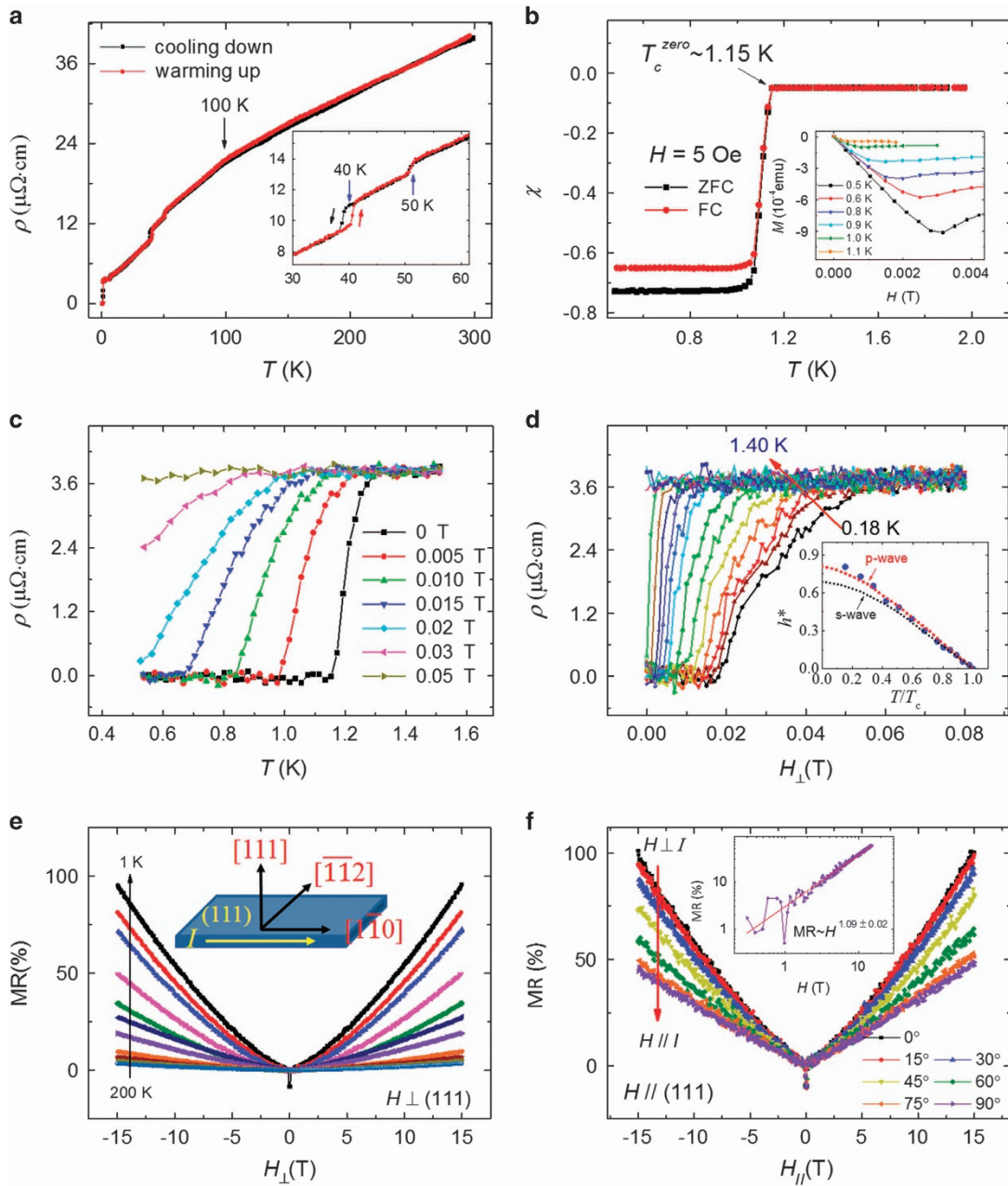


**Figure 2.** Transport measurements of Au<sub>2</sub>Pb. **(a)**  $\rho(T)$  curves of Au<sub>2</sub>Pb single crystal. Inset: close-up of the same data from 30 to 60 K. **(b)** Temperature dependence of  $\chi$ , shows the Meissner effect: sharp diamagnetic drops at 1.15 K. The inset presents low-field  $M(H)$  curves at various temperatures from 0.5 to 1.1 K. **(c)**  $\rho(T)$  characteristics at various  $H_{\perp}$  up to 0.05 T. The  $\rho(T)$  obtained in zero field shows  $T_c^{\text{onset}} = 1.3$  K,  $T_c^{\text{zero}} = 1.18$  K. **(d)** Magnetoresistance of Au<sub>2</sub>Pb crystal at various temperatures under  $H_{\perp}$ . Inset: normalised upper critical field  $h^* = H_{c2}/T_c(dH_{c2}/dT|_{T=T_c})$  as a function of normalised temperature  $t = T/T_c$ , with the red dashed line indicating the expectation for a polar  $p$ -wave state.<sup>19</sup> The black dashed line indicates the WHH theory for  $s$ -wave superconductor.<sup>18</sup> **(e)** MR at temperatures 1, 5, 10, 20, 30, 50, 80, 100, 120, 150 and 200 K measured in  $H_{\perp}$ . **(f)** Parallel magnetic field  $H_{\parallel}$ -dependent resistivity at  $T = 2.5$  K with  $H_{\parallel}$  varying from the 0° to 90°. Inset: MR( $H$ ) curves at 2.5 K for  $H_{\parallel}$  plotted on a logarithmic scale. The linear fitting gives the slope  $\sim 1.09 \pm 0.02$ .

model to be applicable over entire field range. It is noticed that this longitudinal linear MR ( $H_{\parallel}$ ) due to its balanced hole and electron populations, was ever observed in type II Weyl semimetal candidate WTe<sub>2</sub>.<sup>22,29</sup> The linearity here may originate from the multiband nature of Au<sub>2</sub>Pb.

$T_c^{\text{onset}}$  and  $H_{c2}$  enhancements in PC measurement with a W tip PC Andreev reflection spectroscopy is a powerful tool to probe the order parameters of superconductor.<sup>30</sup> The temperature dependence of zero-bias differential resistance of PC between a

gold tip and Au<sub>2</sub>Pb single crystal is shown in Figure 3a. The presence of a significant resistance drop at the onset temperature  $T_c^{\text{onset}} = 1.13$  K at zero magnetic field and the absence of this drop at 0.03 T applied perpendicular to the (111) surface indicate a superconducting transition, which is similar to that in the bulk measured by standard four-electrode method (see Figure 2). However, when measured with a W tip as shown in Figure 3b, the onset temperature increases to 2.1 K, higher than the bulk value. And the perpendicular field ( $H_{\perp}$ ) used to fully suppress the superconductivity transition is 0.755 T, also much higher than the bulk value. The PC spectra (PCS) at different temperatures with a

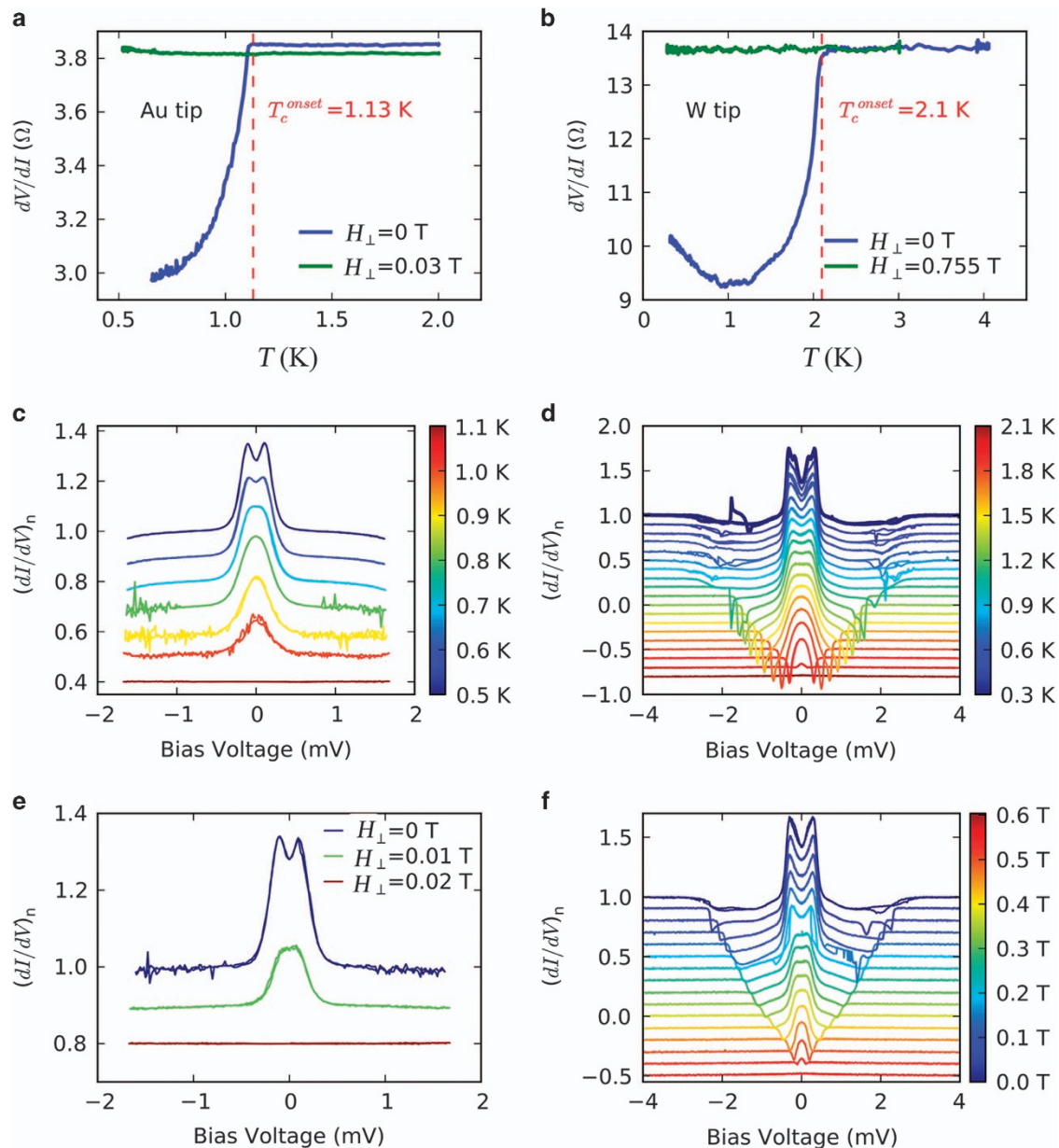


**Figure 3.** PC results with the gold tip and the W tip. **(a, b)** The zero-bias PC resistance as a function of temperature for the gold tip and the W tip, respectively; **(c, d)** the PCS at different  $T$ ; **(e and f)** the PCS under different  $H_{\perp}$  at 0.5 K; curves shifted in **c–f** for clarity.

gold tip and a W tip are shown in Figure 3c,d, respectively. For the PC with a gold tip, DCPs are observed at 0.5 K and gradually get smeared with increasing temperature. The resulted broad conductance peak totally diminishes at 1.1 K, consistent with the transition temperature in  $dV/dI(T)$  as shown in Figure 3a. For the PC with a W tip, similar DCPs feature is clearly shown at lower temperatures, and the broad conductance enhancement totally diminishes at  $T=2.1$  K, consistent with  $T_c^{\text{onset}}$  in Figure 3b. We note that besides the DCPs feature, there are also conductance dips outside the conductance enhancement regime as shown in Figure 3d for temperatures  $>1$  K, which evolve to broad valleys  $<1$  K (around bulk  $T_c$  shown in Figure 2b). These conductance dips might be related to the critical current effect.<sup>31</sup> Alternatively, conductance dips at around the gap energy with a broad ZBCP could be a result of the helical  $p$ -wave order parameter.<sup>32</sup> Another unusual feature of the PCS is a small splitting of the conductance peaks at 0.3 K, which can be fitted by the modified Blonder–Tinkham–Klapwijk (BTK) model<sup>33,34</sup> for two gaps, while

the double conductance dips and broad conductance valleys cannot be fitted by conventional  $s$ -wave pairing symmetry considerations (Supplementary Figure S5).

The magnetic field dependence of PCS at 0.5 K is shown in Figure 3e,f for PC with a gold tip and a W tip, respectively. All the PCS show gradual suppression of the superconducting features with increasing magnetic field. The  $H_{c2}$  for PC with a gold tip is about 0.02 T at 0.5 K, which is close to the bulk value ( $\sim 0.05$  T) obtained by standard four-electrode measurements, while the  $H_{c2}$  value of PC with a W tip is about 0.60 T, which is  $>10$  times larger than the bulk value.

#### Analysis of PC results

For PC with a W tip (harder than gold tip), both  $T_c^{\text{onset}}$  and  $H_{c2}$  are larger than bulk values (Supplementary Figure S6). The  $T_c$  enhancement seems related to the pressure applied by the hard W tips, which may cause changes of the band structure or

lifting of degeneracy of multiple order parameters.<sup>35,36</sup> The conventional cause of  $H_{c2}$  enhancement in PC is the reduction of the mean free path  $l$  in the superconductor as a result of structural defects and/or impurities at interface,<sup>37,38</sup> which leads to a decrease of the coherence length and increase of  $H_{c2}$ . However, this cannot explain the concomitant enhancement of  $T_c$  and  $H_{c2}$  in our situation. In addition, similar superconductivity enhancement for PC with PtIr tips on Au<sub>2</sub>Pb samples was observed, where PtIr tips are also much harder than gold tips. Both the PC results of W tip and PtIr tip suggest that the superconductivity in Au<sub>2</sub>Pb is sensitive to pressure and/or possible doping effect. Magnetoresistance measurements with field applied parallel or perpendicular to sample surface show little anisotropy, which rules out the possibility of surface superconductivity (Supplementary Figure S2).

#### The first-principles calculations

Two important clues in the experimental data are worth remarking. First, for the PCS with a W tip, the double conductance dips feature cannot be adequately described by the BTK theory with *s*-wave pairing symmetry, and points to possible unconventional superconductivity of this material. Second, for transport experimental results, the quasi-linear  $H_{c2}(T)$  data imply the expectation for a *p*-wave state and deviate significantly from the WHH theory for an *s*-wave superconductor. Therefore, it is important to analyse the electronic structure of Au<sub>2</sub>Pb in detail to identify possible unusual topological features.

To examine the effects of PC tip indentation on the sample's local electronic structure, we compare the computed Fermi surfaces of Au<sub>2</sub>Pb of relaxed structure and those under 1% uniaxial strain along the [111] direction. Although the Fermi surfaces are rather complex and appear to be composed of multiple sectors throughout the Brillouin zone (see Supplementary Figure S7), it is evident that the Fermi surfaces are enlarged under

the applied external pressure. The augmentation of Fermi surfaces and the accompanying increase in the density of states at the Fermi energy (shown in Figure 4d) favour higher superconducting  $T_c$ , which agrees with the observed increase of  $T_c$  in the PC measurements. It should also be remarked that the size of Fermi surfaces near the Brillouin zone path  $\Gamma$ -*R* are large and noticeably responsive to external pressure, as shown in Supplementary Figure S7. Thus, in the following, we will focus on the regions near this sector (referred to as the T-sectors hereafter) of the Fermi surfaces.

It is of particular interest to investigate the geometric phase of the bands near the Fermi surfaces. By projecting the Kohn–Sham wavefunctions into various local orbital basis (Supplementary Figure S8), we find that the dominant band components near the Fermi surfaces are parity-even *d*-orbitals of Au and parity-odd *p*-orbitals of Pb. We choose two closed paths on the valence band around one of the T-sectors, and calculate topological invariants through the phase difference,  $\varphi(k) = \arg \langle d|k \rangle - \arg \langle p|k \rangle$ , of the projection coefficients of Kohn–Sham wavefunctions of the highest occupied onto the Au-*d* and Pb-*p* orbitals along these loops. The two loops are carefully chosen to avoid band degeneracy at the band crossing (see the dark blue curve in Figure 5a). In Figure 5b, a unit vector  $n = [\cos \varphi, \sin \varphi]$ , is plotted for each *k*-point on the loop to visualise the orbital texture.

A few interesting features are observed for the projected orbital textures. In particular, the winding numbers are zero for the orbital textures on the inner loop (see e.g., a typical orbital texture on the inner loop in Figure 5b). In contrast, for the outer loop, the orbital textures corresponding to various Au-*d* and Pb-*p<sub>x</sub>* orbitals show a nontrivial topology, with the winding number equals  $-1$ . On the other hand, from Figure 6 we find that an '8' shape projected nodal line is numerically confirmed on a certain Brillouin zone slice, while on another Brillouin zone slice a circle-shaped

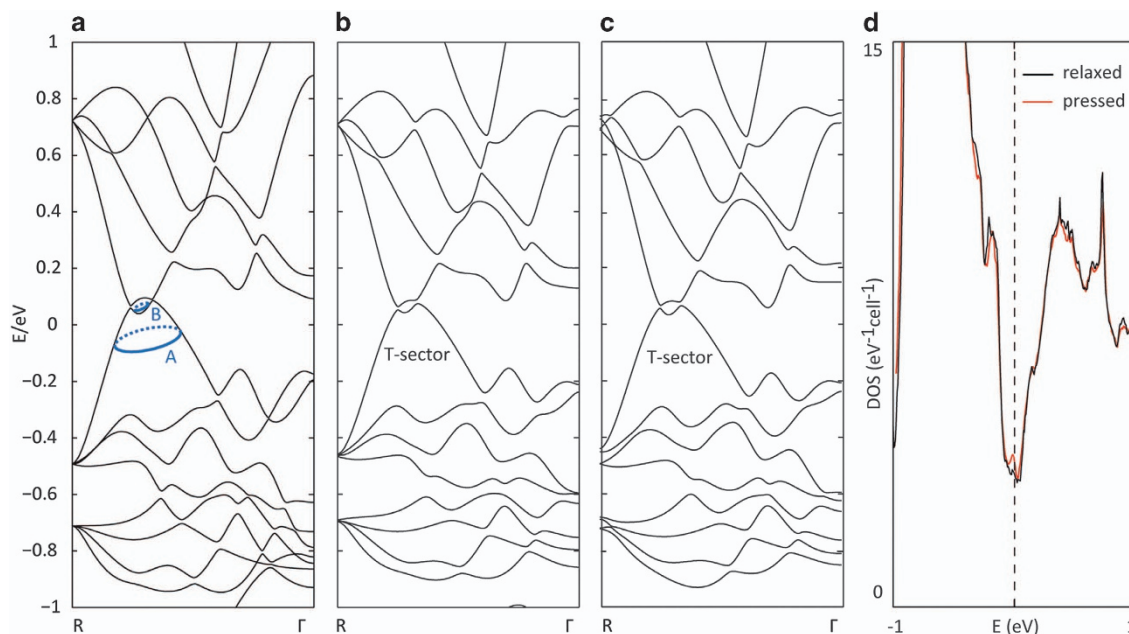


**Figure 4.** The band structures of Au<sub>2</sub>Pb along the Brillouin zone path  $R$ - $\Gamma$ , which undergoes the most obvious change under 1% uniaxial compression. **(a)** Calculation was done with relaxed structure and without spin-orbital coupling. The loop A and loop B correspond to the outer loop and inner loop in Figure 5a, respectively. **(b)** Calculation was done with relaxed structure and with spin-orbit coupling. The result is quite similar to **(a)**. **(c)** Calculation was done with the structure under 1% uniaxial compression and with spin-orbit coupling. The point  $R$  is still defined by  $R = (b_1 + b_2 + b_3)/2$ , as in the case of relaxed structure. Note that the conduction band and the valence band shift to each other as compared with **(b)**. This Brillouin zone region noticeably responsive to external pressure is referred to as the T-sector hereafter, and will be focused on in the investigations of orbital texture. **(d)** Comparison of the density of states of the relaxed structure (black curve) and the compressed structure (red curve). Spin-orbit coupling is included. The density of states near the Fermi level (shifted to 0 eV) is enhanced under the applied external pressure.

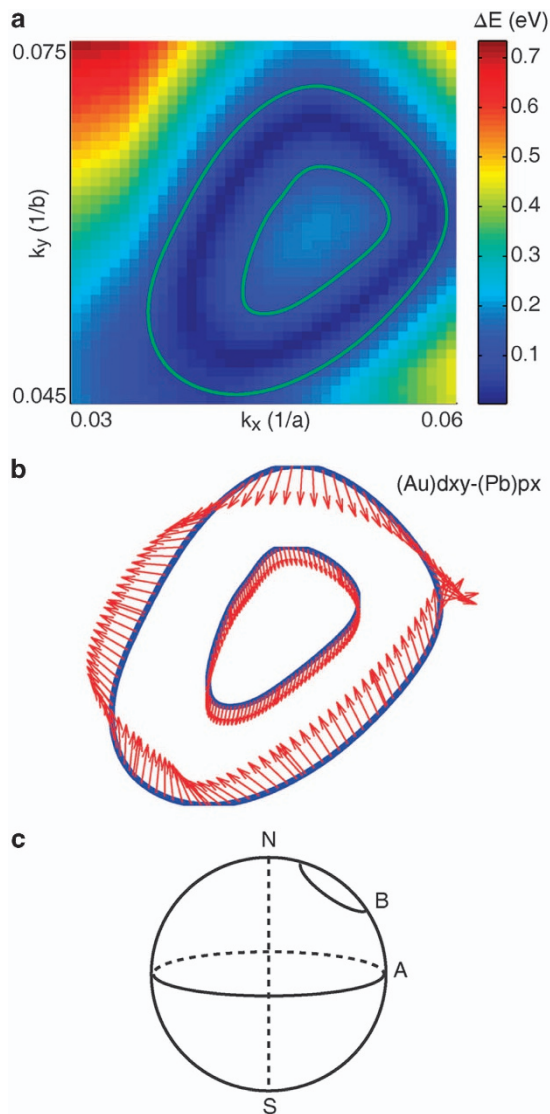


**Figure 5.** Orbital texture of Au<sub>2</sub>Pb. **(a)** A small window of the cross-section  $k_z = 0.69\pi$  (see Figure 6c) of the Brillouin zone, which is near a T-sector. The background colour indicates the energy difference of the conduction band and the valence band (without SOC). Note that there is a dark blue curve on which the conduction band and the valence band are (nearly) degenerate, so the orbital texture will suffer from discontinuity while going across this curve. Based on this consideration, we choose the two green loops, which avoid the degeneracy curve, to calculate the orbital textures. **(b)** The orbital texture of the phase difference of an Au- $d_{xy}$  orbital and a Pb- $p_x$  orbital on the valence band. The direction of the arrows indicates the phase difference of different orbital components of the corresponding wavefunction. The winding number of the orbital texture on the inner loop is 0, and the winding number of the orbital texture on the outer loop is -1. **(c)** The two closed loops partially demonstrate the orbital texture of the effective Hamiltonian (1). The winding number is -1 for the orbital texture on the loop A and is 0 for the loop B, corresponding to the cases of the outer and inner loops in **b**, respectively.

projected nodal line is observed. These intriguing observations hint at nontrivial band structure and topological properties of the T-sectors.

To capture the main features of the band structure around the T-sectors, we introduce an *ad hoc* two-band effective Hamiltonian to describe the physics regarding the Au- $d$  and Pb- $p_x$  orbitals:

$$H_{\text{eff}} = M(k)k \cdot \sigma, \quad (1)$$

where  $k$  denotes the momentum relative to the central point of the '8' shape nodal line shown in Figure 6a, and  $M(k)$  is a polynomial of  $k$ , taken as  $M(k) = m_1 - \sqrt{m_2^2 + k^2}$  with  $m_1 > m_2$ . The energy spectra read  $E_{\pm} = \pm |M(k)k|$ , exhibiting a nodal point at  $k=0$  and a nodal surface at  $k = \sqrt{m_1^2 - m_2^2}$ . One can verify that the above Hamiltonian leads to the band structure and orbital texture consistent with the density functional theory (DFT) calculation results. Actually, the valence band wavefunction of the Hamiltonian is

$$|u_k\rangle = \begin{bmatrix} -\sin \frac{\theta}{2} e^{-i\phi/2} \\ \cos \frac{\theta}{2} e^{i\phi/2} \end{bmatrix}, \quad (2)$$

where  $\theta$  and  $\phi$  are the polar and azimuthal angles of  $k$ , respectively. From the wavefunction, we can see that the orbital texture of the Hamiltonian (1) is determined solely by the  $k \cdot \sigma$  factor. The form of  $M(k)$  has been chosen to mimic the spectra from DFT calculation, reproducing the nodal surface near the Fermi level. It is easy to see that the projected orbital texture is dependent only on  $\phi$  evolved along each path. The orbital texture on any loop that encloses the  $z$  axis ( $k_x = k_y = 0$ ) connecting the north and south poles of the Bloch sphere, has a winding number 1 or -1. In contrast, if the loop excludes the  $z$  axis, the orbital texture is trivial with the winding number being 0. Accordingly, a loop enclosing the nodal line on the  $k_z = \text{constant}$  plane (i.e., the crossing line between the plane with fixed  $k_z$  and the nodal surface) always encloses the  $z$  axis, giving a nonzero winding number of the orbital texture (the outer loop of Figure 5b). However, a loop inside the nodal line may or may not enclose the  $z$  axis. In the latter case, the winding number of the orbital texture is zero, which is understood to be the case of the inner loop of Figure 5b.

## DISCUSSION

The nontrivial topology of the orbital texture suggests the possibility of topological superconductivity. Note that the whole Brillouin zone includes eight different sectors around Fermi energy, with the other seven equivalent copies of the effective Hamiltonian equation (1) obtained by time-reversal and symmetry of the orthogonal space group. In particular, the time-reversal copy of the Hamiltonian (1) can be described by  $\Gamma H_{\text{eff}} \Gamma^{-1} = M(k)[-k_x \sigma_x + k_y \sigma_y - k_z \sigma_z]$ , where the time-reversal operator  $\Gamma = iKs_y$  where  $K$  is the complex conjugate operator, and  $s_y$  is a Pauli matrix operating on real spin. We note that the Hamiltonian equation (1) and its time-reversed copy have opposite spin orientations, which are not explicitly described here. It is readily verified that the topology of the two time-reversed Fermi surfaces is the same. Note that the pairing mechanism cannot annihilate the topological invariants if the Cooper pairs are formed by two Fermi surfaces of the same topology.<sup>39,40</sup> This implies that the superconductivity due to the pairing between such two time-reversed Fermi surfaces is fully gapped and of nontrivial topology inherited from the single-particle states. Due to the time-reversal symmetry, the resulted 3D topological superconductivity is classified by an integer invariant,<sup>41,42</sup> and thus may be stable in the presence of multiple copies of the above paired Hamiltonians in the Brillouin zone.

The combination of transport, diamagnetic, PC measurements and the first-principles calculations are used to study Au<sub>2</sub>Pb crystals. We characterised the superconductivity of Au<sub>2</sub>Pb crystals by transport and diamagnetic experiments. Enhancement of superconductivity is found when it is probed by a hard PC, and we attribute this to local pressure, which is consistent with the enlarged Fermi surface by theoretical calculations. The anomalous quasi-linear  $H_{c2}$  versus  $T$  relation, as well as the gap feature (DCPs with double conductance dips) in PCS, imply possible

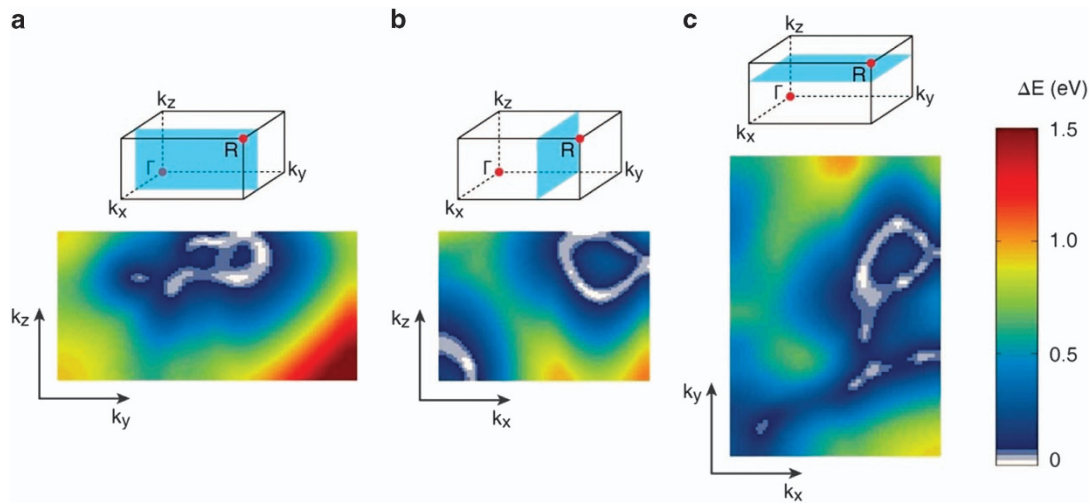


**Figure 6.** Energy difference of the lowest conduction band and the top valence band in the Brillouin zone slices of (a)  $k_y = 0.65\pi$ , (b)  $k_x = 0.65\pi$ , (c)  $k_z = 0.69\pi$ . The top panels show the positions of the corresponding slices within the 1/8 Brillouin zone,  $[0, \pi] \times [0, \pi] \times [0, \pi]$ . Note that the background of Supplementary Figure 8a is a small region in the 2 o'clock direction of c. There are prominent white curves in all these panels, on which the lowest conduction band and the top valence band are nearly degenerate; i.e., these white curves indicate the existence of (quasi) nodal surfaces around the Fermi level.

unconventional superconducting properties in Au<sub>2</sub>Pb crystals. Furthermore, the first-principles calculations point to the nontrivial topology of the orbital texture near the dominant Fermi surfaces, which suggests the possibility of topological superconductivity. The results presented in this work indicate the Au<sub>2</sub>Pb crystal could be a promising platform for the investigation of topological superconductivity. For full understanding of the superconductivity in Au<sub>2</sub>Pb, further investigations like thermal transport and ARPES experiments are clearly necessary and interesting.

#### Note added

After the completion of this work, we notice a recent hydrostatic pressure study of bulk Au<sub>2</sub>Pb,<sup>43</sup> where  $T_c$  decreases with pressure. It is opposite to our observation. The major difference between two studies is that their pressure is hydrostatic but ours is nearly local uniaxial pressure on (111) crystal face.

## MATERIALS AND METHODS

### Sample growth and characterisation

Starting materials of high-purity elemental Au and Pb were prepared to synthesise single-crystalline Au<sub>2</sub>Pb, the initial ratio of Au/Pb was 40:60, the extra Pb were used as flux. The materials were sealed in evacuated quartz ampoules, heated to 600 °C, held for 1 day and then slowly cooled down to 300 °C over a period of 30 h. This was then followed by centrifugation to remove the flux. Before transport and diamagnetic measurements, the samples were etched in a hydrogen peroxide solution for several minutes to remove the residual Pb flux.<sup>16</sup>

The data of powder XRD and single crystal XRD were collected from a Rigaku MiniFlex 600 diffractometer (Rigaku, Tokyo, Japan) and then refined by a Rietica Rietveld programme (<http://www.rietica.org/index.html>). Crystal purity, structure and lattice constant ( $a_1 = a_2 = a_3 = 7.9603 \text{ \AA}$ ) can be retrieved. It is worth to mention that high-quality single crystal of Au<sub>2</sub>Pb samples are in trapezoid stipe shape. The current is added parallel to the bottom edges for transport measurements, which is in  $[1\bar{1}0]$  direction for cubic Laves phase.

To obtain HRTEM images, the Au<sub>2</sub>Pb single crystal was examined by a FEI Tecnai G2 F20 S-TWIN TEM (FEI, Hillsboro, OR, USA) operating at 200 kV.

### Resistivity and diamagnetic measurements

For the transport measurements, the contacts on the single crystals were made by applying the silver paint on the top surface (111) of

Au<sub>2</sub>Pb samples, with contact resistance  $< 1 \Omega$ . The resistance and magnetoresistance were measured in a commercial Physical Property Measurement System (Quantum Design, San Diego, CA, USA, PPMS-16, d.c. technique), with the Helium-3 option for temperature down to 0.5 K and dilution option down to 0.05 K. The excitation current of 1 mA was used for the measurements in low-temperature regime. Angular dependence of magnetoresistance was measured by rotating the sample ((111) surface plane) in a Rotator option based on PPMS, within the instrumental resolution of 0.1°.

For diamagnetic measurement, DC magnetisation was studied during the zero-field cooling and field cooling at  $H = 5 \text{ Oe}$ , in a Magnetic Property Measurement System (MPMS 7-XL SQUID) from Quantum Design Company, with a resolution of  $10^{-8} \text{ e.m.u.}$  The magnetic field is applied parallel to the (111) face. The  $\chi$  is estimated by DC magnetisation.

### The PC measurements

Our PCS are obtained using a standard lock-in technique in quasi-four probe configuration. PC measurements are realized in the standard ‘needle-anvil’ configuration. Both W and gold tips are used to make PC on the (111) surface of Au<sub>2</sub>Pb single crystals. The W tip is prepared by electrochemical etching method with a wire of 0.25 mm diameter, and is hard enough to penetrate through the surface layer and to probe the superconductor underneath. The gold tip is mechanically sharpened from a 0.5 mm wire and is relatively soft.

### The first-principles calculations

The first-principles calculations were performed in the scheme of density-functional theory, as implemented by the VASP package.<sup>44</sup> The projector-augmented wave pseudopotentials<sup>45</sup> were used with Perdew–Burke–Ernzerhof exchange–correlation functional.<sup>46</sup> The energy cutoff of the plane wave basis set was chosen to be 350 eV. The Brillouin zone was sampled by a  $13 \times 19 \times 9$  grid in the self-consistent calculation. During the relaxation procedure, we used a force threshold of  $0.01 \text{ eV \AA}^{-1}$ . Spin-orbit coupling was included in the calculation of energy bands and Fermi surfaces, and not included in the calculation of orbital textures to avoid the twofold degeneracy of the bands to obtain a well-defined phase difference.

## ACKNOWLEDGEMENTS

This work was financially supported by the National Basic Research Programme of China (Grant Nos. 2013CB934600 & 2012CB921300 & 2012CB927400), the Research Fund for the Doctoral Programme of Higher Education (RFDP) of China, the Open Project Programme of the Pulsed High Magnetic Field Facility (Grant No.

PHMFF2015002), Huazhong University of Science and Technology and the National Natural Science Foundation of China (Grant No. 11474008).

## CONTRIBUTIONS

J.W. and J.W. conceived and instructed the experiments. X.Z. and S.J. synthesised and characterised bulk single crystals; Y.X., Y.Z. and Z.W. did the transport experiments; H. W. and J.L. performed the point contact measurement; Y.X., L.L. and M.T. carried out the diamagnetic experiments; J.L. and Y.W. did the TEM characterisation; X.-J.L. contributed to the theoretical interpretation; J.F. and C.-K.L. performed the first-principles calculations.

## COMPETING INTERESTS

The authors declare no conflict of interest.

## REFERENCES

- Young, S. M. *et al.* Dirac semimetal in three dimensions. *Phys. Rev. Lett.* **108**, 140405 (2012).
- Wang, Z. *et al.* Dirac semimetal and topological phase transitions in  $A_3Bi$  ( $A = Na, K, Rb$ ). *Phys. Rev. B* **85**, 195320 (2012).
- Wang, Z., Weng, H., Wu, Q., Dai X & Fang, Z. Three-dimensional Dirac semimetal and quantum transport in  $Cd_3As_2$ . *Phys. Rev. B* **88**, 125427 (2013).
- Liu, Z. K. *et al.* Discovery of a three-dimensional topological dirac semimetal,  $Na_3Bi$ . *Science* **343**, 864–867 (2014).
- Liu, Z. K. *et al.* A stable three-dimensional topological Dirac semimetal  $Cd_3As_2$ . *Nat. Mater.* **13**, 677–681 (2014).
- Neupane, M. *et al.* Observation of a three-dimensional topological Dirac semimetal phase in high-mobility  $Cd_3As_2$ . *Nat. Commun.* **5**, 3786 (2014).
- Jeon, S. *et al.* Landau quantization and quasiparticle interference in the three-dimensional Dirac semimetal  $Cd_3As_2$ . *Nat. Mater.* **13**, 851–856 (2014).
- Xu, S. Y. *et al.* Observation of Fermi arc surface states in a topological metal. *Science* **347**, 294–298 (2015).
- He, L. P. *et al.* Quantum transport evidence for the three-dimensional Dirac semimetal phase in  $Cd_3As_2$ . *Phys. Rev. Lett.* **113**, 246402 (2014).
- Liang, T. *et al.* Ultrahigh mobility and giant magnetoresistance in the Dirac semimetal  $Cd_3As_2$ . *Nat. Mater.* **14**, 280–284 (2015).
- Borisenko, S. *et al.* Experimental realization of a three-dimensional Dirac semimetal. *Phys. Rev. Lett.* **113**, 027603 (2014).
- Xiong, J. *et al.* Evidence for the chiral anomaly in the Dirac semimetal  $Na_3Bi$ . *Science* **350**, 413–416 (2015).
- Wang, H. *et al.* Observation of superconductivity induced by a point contact on 3D Dirac semimetal  $Cd_3As_2$  crystals. *Nat. Mater.* **15**, 38–42 (2016).
- Aggarwal, L. *et al.* Unconventional superconductivity at mesoscopic point contacts on the 3D Dirac semimetal  $Cd_3As_2$ . *Nat. Mater.* **15**, 32–37 (2016).
- He, L. P. *et al.* Pressure-induced superconductivity in the three-dimensional topological Dirac semimetal  $Cd_3As_2$ , Preprint at <http://arxiv.org/abs/1502.02509> (2015).
- Schoop, L. M. *et al.* Dirac metal to topological metal transition at a structural phase change in  $Au_2Pb$  and prediction of  $Z_2$  topology for the superconductor. *Phys. Rev. B* **91**, 214517 (2015).
- Hamilton, D. C., Raub, C. H. & Matthias, B. T. Some new superconducting compounds. *J. Phys. Chem. Solids* **26**, 665–667 (1965).
- Werthamer, N. R., Helfand, E. & Hohenberg, P. C. Temperature and purity dependence of the superconducting critical field,  $H_{c2}$ . III. electron spin and spin-orbit effects. *Phys. Rev.* **147**, 295–302 (1966).
- Scharnberg, K. & Klemm, R. A. p-wave superconductors in magnetic fields. *Phys. Rev. B* **22**, 5233 (1980).
- Nakajima, Y. *et al.* Topological RPDi half-Heusler semimetals: a new family of noncentrosymmetric magnetic superconductors. *Sci. Adv.* **1**, 5 (2016).
- Xu, R., Husmann, A., Rosenbaum, T. F., Saboungi, M. L. & Enderby, J. E. Large magnetoresistance in non-magnetic silver chalcogenides. *Nature* **390**, 57–60 (1997).
- Zhao, Y. *et al.* Anisotropic magnetotransport and exotic longitudinal linear magnetoresistance in  $WTe_2$  crystals. *Phys. Rev. B* **92**, 041104(R) (2015).
- Zhang, W. *et al.* Topological aspect and quantum magnetoresistance of  $\beta\text{-Ag}_2\text{Te}$ . *Phys. Rev. Lett.* **106**, 156808 (2011).
- Tang, H., Liang, D., Qiu, R. L. & Gao, X. P. Two-dimensional transport-induced linear magneto-resistance in topological insulator  $Bi_2Se_3$  nanoribbons. *ACS Nano* **5**, 7510–7516 (2011).
- Zhao, Y. *et al.* Demonstration of surface transport in a hybrid  $Bi_2Se_3/Bi_2Te_3$  heterostructure. *Sci. Rep.* **3**, 3060 (2013).
- Zhao, Y. *et al.* Anisotropic fermi surface and quantum limit transport in high mobility three-dimensional dirac semimetal  $Cd_3As_2$ . *Phys. Rev. X* **5**, 031037 (2015).
- Narayanan, A. *et al.* Linear magnetoresistance caused by mobility fluctuations in n-doped  $Cd_3As_2$ . *Phys. Rev. Lett.* **114**, 117201 (2015).
- Abrikosov, A. A. Quantum magnetoresistance. *Phys. Rev. B* **58**, 2788–2794 (1998).
- Solyuyanov, A. A. *et al.* Type-II Weyl semimetals. *Nature* **527**, 495–498 (2015).
- Deutscher, G. Andreev-Saint-James reflections: a probe of cuprate superconductors. *Rev. Mod. Phys.* **77**, 109–135 (2005).
- Sheet, G., Mukhopadhyay, S. & Raychaudhuri, P. Role of critical current on the point-contact andreev reflection spectra between a normal metal and a superconductor. *Phys. Rev. B* **69**, 134507 (2004).
- Kashiwaya, S., Kashiwaya, H., Saitoh, K., Mawatari, Y. & Tanaka, Y. Tunneling spectroscopy of topological superconductors. *Phys. E* **55**, 25–29 (2014).
- Blonder, G. E., Tinkham, M. & Klappwijk, T. M. Transition from metallic to tunneling regimes in superconducting microconstrictions: Excess current, charge imbalance, and supercurrent conversion. *Phys. Rev. B* **25**, 4515 (1982).
- Daghero, D. & Gonnelli, R. S. Probing multiband superconductivity by point-contact spectroscopy. *Supercond. Sci. Technol.* **23**, 043001 (2010).
- Hicks, C. W. *et al.* Strong increase of  $t_c$  of  $Sr_2RuO_4$  under both tensile and compressive strain. *Science* **344**, 283–285 (2014).
- Wang, H. *et al.* Enhanced superconductivity at the interface of  $W/Sr_2RuO_4$  point contacts. *Phys. Rev. B* **91**, 184514 (2015).
- Naidyuk, Y. G., Häussler, R. & Löhneysen, H. V. Magnetic field dependence of the andreev reflection structure in the conductivity of s-n point contacts. *Phys. B Condens. Matter* **218**, 122–125 (1996).
- Miyoshi, Y., Bugoslavsky, Y., Minakov, A. A., Blamire, M. G. & Cohen, L. F. Local enhancement of the upper critical field in niobium point contacts. *Supercond. Sci. Technol.* **18**, 1176 (2005).
- Kitaev, A. Periodic table for topological insulators and superconductors. *AIP Conf. Proc.* **1134**, 22 (2009).
- Qi, X. L., Hughes, T. L. & Zhang, S. C. Topological invariants for the Fermi surface of a time-reversal-invariant superconductor. *Phys. Rev. B* **81**, 134508 (2010).
- Kobayashi, S. & Sato, M. Topological superconductivity in dirac semimetals. *Phys. Rev. Lett.* **115**, 187001 (2015).
- Schnyder, A. P., Ryu, S., Furusaki, A. & Ludwig, A. W. Classification of topological insulators and superconductors in three spatial dimensions. *Phys. Rev. B* **78**, 195125 (2008).
- Chen, K. W. *et al.* Temperature-pressure phase diagram of cubic Laves phase  $Au_2Pb$ . *Phys. Rev. B* **93**, 045118 (2016).
- Kresse, G. & Furthmüller, J. Efficient iterative schemes for ab initio total-energy calculations using a plane-wave basis set. *Phys. Rev. B* **54**, 11169 (1996).
- Kresse, G. & Joubert, D. From ultrasoft pseudopotentials to the projector augmented-wave method. *Phys. Rev. B* **59**, 1758 (1999).
- Perdew, J. P., Burke, K. & Ernzerhof, M. Generalized gradient approximation made simple. *Phys. Rev. Lett.* **77**, 3865 (1996).



This work is licensed under a Creative Commons Attribution 4.0 International License. The images or other third party material in this article are included in the article's Creative Commons license, unless indicated otherwise in the credit line; if the material is not included under the Creative Commons license, users will need to obtain permission from the license holder to reproduce the material. To view a copy of this license, visit <http://creativecommons.org/licenses/by/4.0/>

© The Author(s) 2016

Supplementary Information accompanies the paper on the *npj Quantum Materials* website (<http://www.nature.com/npjquantumats>)